

Crystal structures of $\text{NiSO}_4 \cdot 9\text{H}_2\text{O}$ and $\text{NiSO}_4 \cdot 8\text{H}_2\text{O}$: magnetic properties, stability with respect to morenosite ($\text{NiSO}_4 \cdot 7\text{H}_2\text{O}$), the solid-solution series $(\text{Mg}_x\text{Ni}_{1-x})\text{SO}_4 \cdot 9\text{H}_2\text{O}$

A. D. Fortes^{1,2}  · K. S. Knight^{1,2,3} · A. S. Gibbs¹ · I. G. Wood²

Received: 4 December 2017 / Accepted: 17 February 2018 / Published online: 23 February 2018
© The Author(s) 2018. This article is an open access publication

Abstract

Since being discovered initially in mixed-cation systems, a method of forming end-member $\text{NiSO}_4 \cdot 9\text{H}_2\text{O}$ and $\text{NiSO}_4 \cdot 8\text{H}_2\text{O}$ has been found. We have obtained powder diffraction data from protonated analogues (with X-rays) and deuterated analogues (using neutrons) of these compounds over a range of temperatures, allowing us to determine their crystal structures—including all H-atoms—and to characterise the transitions on warming from 220 to 278 K; glass → 9-hydrate → 8-hydrate + ice → 7-hydrate + ice → partial melt (7-hydrate + liquid). $\text{NiSO}_4 \cdot 8\text{D}_2\text{O}$ is triclinic, space-group $P\bar{1}$, $Z=2$, with unit cell parameters at 150 K, $a=6.12463(8)$ Å, $b=6.8401(1)$ Å, $c=12.5339(2)$ Å, $\alpha=92.846(1)^\circ$, $\beta=97.822(1)^\circ$, $\gamma=96.627(1)^\circ$ and $V=515.58(1)$ Å³. The structure consists of two symmetry-inequivalent $\text{Ni}(\text{D}_2\text{O})_6$ octahedra on sites of $\bar{1}$ symmetry. These are directly joined by a water–water H-bond to form chains of octahedra parallel with the c -axis at $x=0$. Two interstitial water molecules serve both to bridge the $\text{Ni}(\text{D}_2\text{O})_6$ octahedral chains in the b – c plane and also to connect with the SO_4^{2-} tetrahedral oxyanion. These tetrahedra are linked by the two interstitial water molecules in a reticular motif to form sheets perpendicular to c . $\text{NiSO}_4 \cdot 9\text{D}_2\text{O}$ is monoclinic, space-group $P2_1/c$, $Z=4$, with unit-cell parameters at 150 K, $a=6.69739(6)$ Å, $b=11.8628(1)$ Å, $c=14.5667(1)$ Å, $\beta=94.9739(8)^\circ$ and $V=1152.96(1)$ Å³. The structure is isotopic with the Mg analogue described elsewhere (Fortes et al., Acta Cryst B 73:47–64, 2017b). It shares the motif of H-bonded octahedral chains with $\text{NiSO}_4 \cdot 8\text{D}_2\text{O}$, although in the enneahydrate these run parallel with the b -axis at $x=0$. Three interstitial water molecules bridge the $\text{Ni}(\text{D}_2\text{O})_6$ octahedra to the SO_4^{2-} tetrahedral oxyanion. The tetrahedra sit at $x \approx 0.5$ and are linked by two of the three interstitial water molecules in a pentagonal motif to form ribbons parallel with b . A solid-solution series exists between Mg and Ni enneahydrate end-members where we observe preferential partitioning of Ni^{2+} into the octahedral sites on the 2c Wyckoff positions rather than the 2a sites. The solution is slightly non-ideal, as indicated by the small positive excess volume of mixing. Measurements of the DC magnetisation of quenched NiSO_4 solutions reveal anomalies in the molar susceptibility on warming through the region from 221 to 225 K, probably due to devitrification of the (assumed) glassy specimen into a mixture of $\text{NiSO}_4 \cdot 9\text{H}_2\text{O}$ + ice Ih. Further temperature-dependent measurements on repeated warming and cooling provide no evidence of magnetic ordering and indicate a weak ferromagnetic coupling between neighbouring Ni^{2+} ions, likely via super-exchange through the H-bond between neighbouring $\text{Ni}(\text{H}_2\text{O})_6$ octahedra.

Keywords NiSO_4 · Enneahydrate · Octahydrate · Solid solution · Neutron diffraction · DFT

Introduction

Background

Crystalline hydrates having the general formula $\text{NiSO}_4 \cdot n\text{H}_2\text{O}$ with $n=1, 2, 3, 4, 5, 6$, and 7 are well known (Chrétien and Rohmer 1934), some of which occur naturally as the minerals dwornikite ($n=1$, with ~10 atom % Fe^{2+}), retgersite and nickelhexahydrite (tetragonal and monoclinic polymorphs with $n=6$), and morenosite ($n=7$), respectively. As part of a

Electronic supplementary material The online version of this article (https://doi.org/10.1007/s00269-018-0956-z) contains supplementary material, which is available to authorized users.

✉ A. D. Fortes
dominic.fortes@stfc.ac.uk

Extended author information available on the last page of the article

broader programme of research into water-rich cryohydrates, we attempted to synthesise compounds having $n > 7$ with the specific aims of identifying a hypothetical Ni-analogue of meridianiite ($\text{MgSO}_4 \cdot 11\text{H}_2\text{O}$) or of isolating hitherto unknown hydrates with $7 < n < 11$. Whilst we failed to form the $\text{NiSO}_4 \cdot 11\text{H}_2\text{O}$ end-member, we succeeded instead in producing a novel hydrate with $n = 9$ in systems containing mixtures of Ni, Zn or Fe with Mg, and a new hydrate with $n = 8$ in pure NiSO_4 (Fortes et al. 2012a, b). Since then, we have been able to form end-member 9-hydrates from each of MgSO_4 , NiSO_4 and ZnSO_4 . However, it remains the case that the octahydrate has been observed solely in NiSO_4 -bearing mixtures.

There have been a few prior reports in the literature concerning octahydrates of divalent metal sulfates, including Mg^{2+} (Takegami 1922) and Fe^{2+} (Viola 1923) although these were shown subsequently to be either irreproducible or due to errors of analysis (Benrath and Schröder 1927; D'Ans 1933). In light of this, we were quite cautious in our assertion that the newly identified hydrate of NiSO_4 was an octahydrate based solely on molar volume considerations. Since we consider the formation of a single-phase and ice-free specimen of $\text{NiSO}_4 \cdot 8\text{H}_2\text{O}$ to be practically impossible by flash-freezing of a stoichiometric aqueous solution, and since the metastability of this phase precludes growth, extraction or handling of even small crystals suitable for either X-ray single-crystal diffraction or thermogravimetric analysis, the only way to confirm the stoichiometry is to solve the structure from mixed-phase powder diffraction data. In achieving that goal we will show that this phase is indeed an octahydrate; along with the structure refinement of nickel sulfate enneahydrate reported in this work, these are the first new NiSO_4 hydrate structures to be established with certainty in over 80 years.

Characterising the structures, properties and phase behaviour of these new cryohydrates sheds fresh light on a little-explored but pertinent area of (principally extraterrestrial) mineralogy. Exploration of Mars and of the outer solar system over the past five decades has revealed the importance of aqueous solutions, or brines, which result in the possible deposition of a great variety of polyhydrated inorganic salts on planetary surfaces. Since these environments are typically much colder than the Earth's mean surface temperature, the behaviour of such brines when crystallised at low temperatures—even flash frozen, as may occur on extrusion or spraying into the ultra-cold surface environment of an outer solar system body—is important to understand. This is reflected in the efforts of the planetary science community to determine experimentally which stable or metastable phases appear when different brine compositions are frozen at different rates (e.g., Hennings et al. 2013; Schmidt et al. 2013; Toner et al. 2014; Vu et al. 2016, 2017; Thomas et al. 2017) or when salt hydrates are exposed to elevated relative

humidities at low temperatures (Leftwich et al. 2013). Our work on divalent metal sulfate cryohydrates adds a small piece to this larger picture.

This work forms the final part of a series of three closely related papers. The first deals with the high-pressure behaviour of meridianiite ($\text{MgSO}_4 \cdot 11\text{H}_2\text{O}$) and its decomposition to $\text{MgSO}_4 \cdot 9\text{H}_2\text{O}$ (Fortes et al. 2017a); the second paper reports on the structure and thermoelastic properties of $\text{MgSO}_4 \cdot 9\text{H}_2\text{O}$ (Fortes et al. 2017b). This third paper deals purely with the structures and properties of $\text{NiSO}_4 \cdot 9\text{H}_2\text{O}$ and $\text{NiSO}_4 \cdot 8\text{H}_2\text{O}$.

Experimental objectives

The objectives of this work are: (i) to refine the crystal structure of $\text{NiSO}_4 \cdot 9\text{H}_2\text{O}$, including all hydrogen positions, based on the recently determined structure of $\text{MgSO}_4 \cdot 9\text{H}_2\text{O}$; (ii) to determine the crystal structure of $\text{NiSO}_4 \cdot 8\text{H}_2\text{O}$; (iii) to establish the relative stability of these phases with respect to one another and to $\text{NiSO}_4 \cdot 7\text{H}_2\text{O}$ as a function of temperature; (iv) to characterise the variation in unit cell parameters across the solid-solution series between $\text{MgSO}_4 \cdot 9\text{H}_2\text{O}$ and $\text{NiSO}_4 \cdot 9\text{H}_2\text{O}$ and relate this to the site distribution of Ni^{2+} in the structure, and (v) to characterise the magnetic properties, where possible, of these hydrates for comparison with literature data on the hepta- and hexahydrates.

Experimental methods

Sample synthesis

Aqueous solutions for the X-ray powder diffraction measurements were prepared from $\text{NiSO}_4 \cdot 7\text{H}_2\text{O}$ (Sigma-Aldrich 72285, purum > 99.0 wt%) dissolved in H_2O (Alfa-Aesar, ACS Reagent Grade, 36645); for the neutron powder diffraction measurements, solutions were prepared from anhydrous NiSO_4 (Aldrich 656895, 99.99% trace metals basis) dissolved in D_2O (Aldrich 151882 99.9 atom % D). Additionally, mixtures of anhydrous powder with the composition $(\text{Mg}_x\text{Ni}_{1-x})\text{SO}_4$ were prepared in the range $1 < x < 0.1$ in increments of 0.1, which were also dissolved in D_2O . All of the solutions were prepared with a concentration of 25 wt% anhydrous solid. These liquids were pipetted as droplets directly into $\sim 30 \text{ cm}^3$ of liquid nitrogen held in a steel cryo-mortar ($\varnothing = 60 \text{ mm}$, depth 20 mm), producing glassy solid spherules in the region of 2–4 mm in diameter. The amorphous spherules were pulverised with a nitrogen-chilled steel pestle and mortar and then transferred to an appropriate sample holder. This work was carried in the UCL Earth Sciences Cold Rooms at an air temperature of around 260 K.

X-ray powder diffraction

X-ray powder diffraction data were obtained using a PANalytical X'Pert Pro multipurpose powder diffractometer with germanium monochromated CoK α_1 radiation ($\lambda = 1.788996 \text{ \AA}$, and an X'Celerator multi-strip detector). Data were collected with variable divergence and receiving slits, converted to fixed-slit geometry with the proprietary X'Pert Pro HighScore Plus software package, and exported in an appropriate format for analysis in the GSAS/Expgui package (Larsen and Von Dreele 2000; Toby 2001).

Low-temperature measurements were achieved using a thermoelectrically cooled sample stage (Wood et al. 2012). The cold stage was held in a plastic box filled with dry-ice pellets whilst the powder specimen was prepared and loaded. Powder samples were transferred to the cold stage and packed down to form a top-loaded pressed-powder specimen.

Measurements of quench-frozen $[\text{Mg}_x\text{Ni}_{1-x}]\text{SO}_4$ cryohydrates were made at temperatures between 258 and 261 K. The limitations imposed by the operating temperature of the Peltier stage meant that only mixtures containing ≥ 90 atom % Ni formed the triclinic crystal that we inferred (on the basis of molar volume considerations) to be an octahydrate; lower nickel concentrations produced a monoclinic enneahydrate and eventually, for $\text{Ni} < 40$ atom %, the triclinic $(\text{Mg},\text{Ni})\text{SO}_4 \cdot 11\text{H}_2\text{O}$ (Ni-meridianite). A representative X-ray powder diffraction pattern from $\text{NiSO}_4 \cdot 8\text{H}_2\text{O}$ is shown in Fig. 1.

The analysis of these X-ray data is largely presented in our earlier work (Fortes et al. 2012a, b). Following the neutron diffraction and computational studies described in the

following sections, we have re-evaluated some of the X-ray data, in particular the dataset measured at 259.95 K on end-member $\text{NiSO}_4 \cdot 8\text{H}_2\text{O}$ (Fig. 1) and the 40 wt% Ni dataset measured at 257.75 K (see Fig. 9).

Neutron powder diffraction

Neutron powder diffraction data were collected using the high resolution powder diffractometer (HRPD) (Ibberson et al. 1992; Ibberson 2009) at the STFC ISIS spallation neutron source, Rutherford Appleton Laboratory, UK, which is ideally suited to rapid, accurate and precise determination of unit-cell parameters by virtue of its long neutron flight path (95 m) and essentially Q -independent resolution; $\Delta d/d \approx 6 \times 10^{-4}$ in the backscattering detectors, $2\theta = 168.33^\circ$.

Samples of $\text{NiSO}_4 \cdot 8\text{D}_2\text{O} + \text{ice}$ were prepared by quenching of large globules of aqueous NiSO_4 in liquid nitrogen to form solid ‘buttons’ with a diameter of ~ 20 mm and a thickness of ~ 5 mm. These were stored overnight in a freezer at 255 K before being powdered under liquid nitrogen in a steel cryomortar and then loaded into a pre-cooled sample holder mounted on a cryostat centre stick. The sample holder consisted of an aluminium frame with a slab-geometry cavity of width 18 mm, height 23 mm and depth (parallel to the incident beam) 15 mm. Steel-framed vanadium windows were screwed to the front and back of the holder, the exposed Al and steel components on the front face being masked by Gd and Cd foils. After installation on the beamline, the temperature was reduced to 150 K. The specimen was measured for 8 h in HRPD’s 30–130 ms time-of-flight (t-o-f) window, taken off the beamline and stored in dry-ice for 1 day whilst another sample was studied, and then re-loaded at 150 K for a 3.25 h measurement in the 100–200 ms t-o-f window.

Shorter annealing times in the freezer (< 1 h) were found to produce samples containing principally $\text{NiSO}_4 \cdot 9\text{D}_2\text{O}$. We considered it useful, therefore, to observe the annealing process *in situ* as a function of temperature. To this end, a solid quench sample was loaded into a slab-can at liquid nitrogen temperatures and neutron powder diffraction data were collected as it was warmed up to the point of devitrification (220 K). At this point the sample was observed to consist of a phase mixture, comprising ice Ih and $\text{NiSO}_4 \cdot 9\text{D}_2\text{O}$. Data were subsequently collected on warming in 5 K increments to 260 K and then 2 K increments up to 278 K for 1 h each in the 100–200 ms t-o-f window.

Complementary datasets were obtained from flash-frozen mixtures of aqueous MgSO_4 with NiSO_4 . These were prepared and loaded under liquid nitrogen in the same manner as above and mounted in a cryostat on HRPD at 150 K. Warming to ca. 220 K induced crystallisation of $(\text{Mg}_{1-x}\text{Ni}_x)\text{SO}_4 \cdot 9\text{D}_2\text{O}$. Solutions prepared with x varying from 0 to 1 in 0.1 atom-fraction increments were crystallised

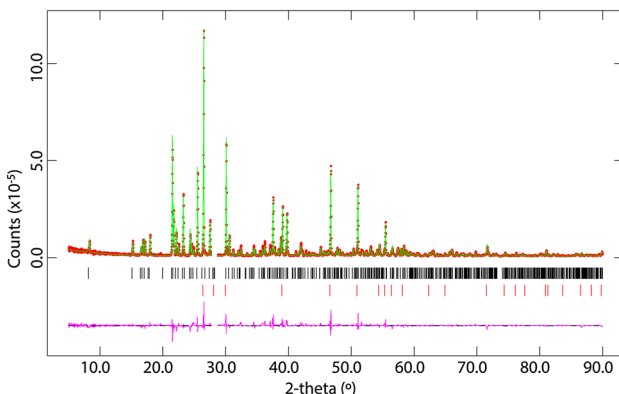


Fig. 1 Representative X-ray powder diffraction pattern of $\text{NiSO}_4 \cdot 8\text{D}_2\text{O}$ measured at 260 K. Filled red circles report the observed data, solid green lines the calculated fit based on a joint refinements of the X-ray and neutron diffraction data (see text); the purple line underneath is Obs-Calc. Tick marks for $\text{NiSO}_4 \cdot 8\text{D}_2\text{O}$ are uppermost and those for water ice are below them. A small excluded region near $2\theta = 28^\circ$ covers an ill-fitted ice Bragg peak

as outlined previously and then cooled to 150 K for acquisition of 1 h datasets in HRPD's 100–200 ms time window. Above $x=0.3$, these specimens comprised $(\text{Mg}_{1-x}\text{Ni}_x)\text{SO}_4\cdot9\text{D}_2\text{O} + \text{ice}$; samples with $x=0.4, 0.5$ and 0.8 contained small but non-negligible contributions from the octahydrate, $(\text{Mg}_{1-x}\text{Ni}_x)\text{SO}_4\cdot8\text{D}_2\text{O}$.

All powder diffraction data were normalised to the incident spectrum and corrected for detector efficiency using data from a vanadium standard. Representative neutron powder diffraction patterns from $\text{NiSO}_4\cdot9\text{D}_2\text{O}$ are shown in Fig. 2. A summary of the neutron powder diffraction datasets used in this work is provided in Table 1.

Magnetic property measurements

Measurements of the magnetic properties of (inferred) $\text{NiSO}_4\cdot9\text{H}_2\text{O} + \text{ice}$ mixtures were obtained using a commercial SQUID magnetometer (Quantum Design MPMS-7T, McElfresh 1994). Approximately 200 mg of aqueous solution containing 27.14 wt% NiSO_4 was loaded into a gelatine

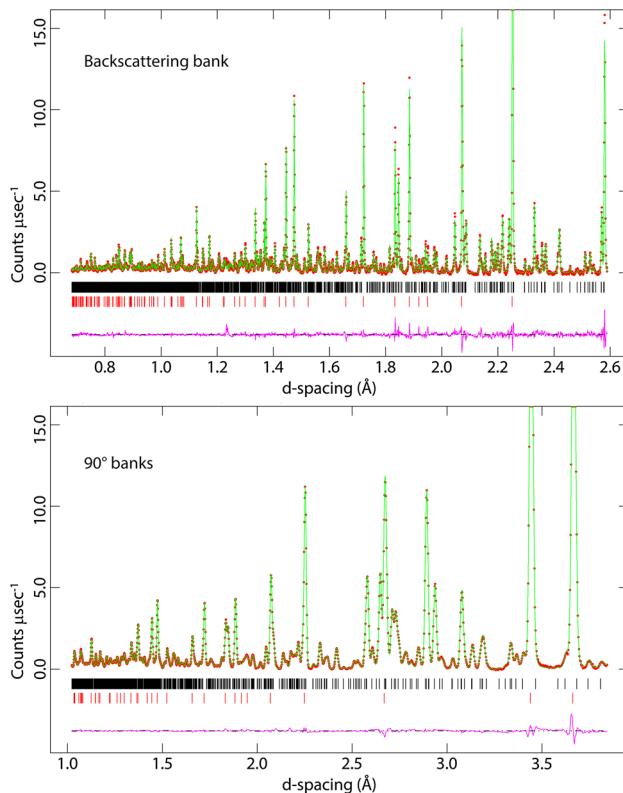


Fig. 2 Rietveld refinement of the $\text{NiSO}_4\cdot9\text{D}_2\text{O}$ structure against neutron powder diffraction data obtained at 150 K in HRPD's 30–130 ms window. The left-hand panel shows the data measured in the back-scattering detector banks and the right-hand panel shows data from the 90° detectors in the same time window. Filled red circles report the observed data, solid green lines the calculated fit and the purple line underneath is Obs-Calc. Tick marks for $\text{NiSO}_4\cdot9\text{D}_2\text{O}$ are uppermost and those for water ice are below them

capsule (mass ≈ 37 mg) and mounted on the SQUID sample stick inside a polyethylene straw. The specimen capsule was then inserted into the instrument chamber where it was immersed in He exchange gas at 80 K; our in situ diffraction observations, outlined in “Neutron powder diffraction”, led us to believe that this would result in a glassy specimen, which would devitrify on warming through 220 K.

DC mass-susceptibility measurements were then made in a 1 kOe applied field as the sample temperature was reduced to 2 K (at 3 K min⁻¹), increased from 2 to 200 K at the same rate and then warmed more slowly from 200 to 240 K (1 K min⁻¹). A significant drop in the susceptibility was observed between 224 and 227 K (Fig. 3), which we attribute to the crystallisation of $\text{NiSO}_4\cdot9\text{H}_2\text{O}$ from a glassy precursor. In order to test this hypothesis, the temperature program was repeated, cooling to 2 K and back up to 240 K; no further anomalies were detected, supporting our interpretation of the susceptibility drop as a signature of devitrification.

A second and third loading of the same aqueous solution was carried out to evaluate the effect of a larger applied field and of different temperature ramp rates. Sample #2 was studied in a 10 kOe field, being cooled from 80 to 2 K and then warmed from 2 to 220 K at 3 K min⁻¹. Over the range where we expected devitrification to occur (220–230 K), the ramp was reduced to 0.2 K min⁻¹. As in Sample #1, there was a drop in the susceptibility, but the feature was much narrower and at a slightly lower temperature, peaking at 221.3 K and extending from 220.4 to 222.0 K. As before, continued temperature cycling revealed no further anomalies.

Sample #3 was measured in a 1 kOe applied field, but data acquisition was done with a thermal equilibration wait time at each datum instead of measuring on a continuous temperature ramp. The effect of this was to reproduce the lower temperature of the devitrification anomaly seen in Sample #2 but to greatly reduce its magnitude. Finally, a magnetic hysteresis loop was measured at 2 K in the range ± 70 kOe.

Data were corrected for the susceptibility of the gel capsule and the core diamagnetism of NiSO_4 (Bain and Berry 2008) and ice (Senftle and Thorpe 1962) in the specimen and converted to inverse molar susceptibility, $1/\chi_m$, for further analysis.

Density functional theory calculations

In order to aid in the interpretation of some of our experimental data we carried out a series of first-principles calculations using density functional theory, DFT, and the plane-wave pseudopotential method (Hohenberg and Kohn 1964; Kohn and Sham 1965). The calculations were carried out using CASTEP (Payne et al. 1992; Segall et al. 2002; Clark et al. 2005) in conjunction with the analysis tools in the Materials Studio software package (<http://accelrys.com>).

Table 1 Details of the experimental conditions for each neutron powder diffraction dataset

| Sample ID (atom % Ni) | Experimental run number | Temperature (K) | Time-of-flight window (ms) | Counting time ^a (μ A h) | Majority hydrate phase |
|--|-------------------------|-----------------|----------------------------|------------------------------------|------------------------|
| Mixed (Mg,Ni)SO ₄ hydrate compositional series | | | | | |
| 10 | 51712 | 150 | 30–130 | 50 | 11-Hydr |
| 20 | 51714 | ” | ” | ” | ” |
| 30 | 51716 | ” | ” | ” | 9-Hydr |
| 40 | 51721 | ” | ” | ” | ” |
| 50 | 51718 | ” | ” | 30 | ” |
| 50 | 51719 | ” | 100–200 | 280 | ” |
| 60 | 51723 | ” | 30–130 | 50 | ” |
| 70 | 51725 | ” | ” | ” | ” |
| 80 | 51727 | ” | ” | 70 | ” |
| 90 | 51752 | ” | ” | 50 | ” |
| 100 | 51731 → 51750 | ” | ” | 380 | ” |
| 100 | 51755 → 51770 | ” | ” | 300 | 8-Hydr |
| 100 | 51786 | ” | 100–200 | 120 | ” |
| Temperature-dependent series for pure NiSO ₄ end-member | | | | | |
| 100 | 55649 | 200 | 100–200 | 39 | None |
| ” | 55650 | 225 | ” | 35 | 9-Hydr |
| ” | 55651 | 230 | ” | ” | ” |
| ” | 55652 | 235 | ” | ” | ” |
| ” | 55653 | 240 | ” | ” | ” |
| ” | 55654 | 245 | ” | ” | ” |
| ” | 55655 | 250 | ” | ” | 8-Hydr |
| ” | 55656 | 255 | ” | ” | ” |
| ” | 55657 | 260 | ” | ” | ” |
| ” | 55658 | 262 | ” | ” | ” |
| ” | 55659 | 264 | ” | ” | ” |
| ” | 55660 | 266 | ” | ” | ” |
| ” | 55661 | 268 | ” | ” | ” |
| ” | 55662 | 270 | ” | ” | ” |
| ” | 55663 | 272 | ” | ” | ” |
| ” | 55664 | 274 | ” | ” | 7-Hydr |
| ” | 55664 | 276 | ” | ” | ” |
| ” | 55666 | 278 | ” | 15 | None |

These data comprise ISIS experiment RB1120190 “Cation substitution in synthetic meridianite (MgSO₄·11D₂O): phase behaviour and changes in unit-cell parameters” for which the raw uncorrected data (and associated meta-data) are now publicly available in the ISIS Data Catalogue (<http://www.isis.stfc.ac.uk/Pages/ICAT.aspx>). The experiment archive may be located via the <https://doi.org/10.5286/ISIS.E.24088565> and specific datasets can be found using the run numbers tabulated here. A series of run numbers indicates that all measurements in the specified range were summed together

Tests for convergence of the total energy and of structural parameters were done by varying the basis-set cut-offs and the reciprocal-space sampling. As described in our earlier paper (Fortes et al. 2017b), we found that the recently developed Wu–Cohen GGA functional (Wu and Cohen 2006) gives more accurate structural parameters than PBE for these materials, changing the ~5% over-estimation of molar volume to a ~1% under-estimation.

Using the WC GGA with ultrasoft pseudopotentials (non-linear core-corrected for Ni) with a basis-set cut-off of

1200 eV and a $4 \times 2 \times 2 \vec{k}$ -point grid for the 9-hydrate and a $3 \times 3 \times 2 \vec{k}$ -point grid for the 8-hydrate (~0.04 Å⁻¹ reciprocal lattice spacing in both cases) achieved a satisfactory convergence of the total energy.

Spin-polarised calculations were done for the Ni-bearing compounds so as to allow degenerate *d*-orbitals to adopt differing energy levels, these being done for a variety of ferromagnetic and antiferromagnetic initial spin configurations. For simplicity, the quantisation axis (or spin direction)

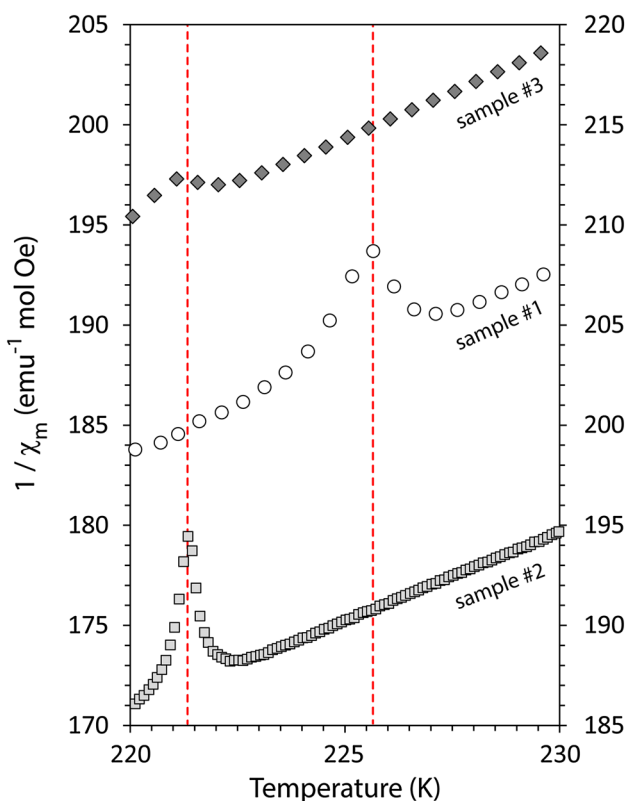


Fig. 3 Expanded view of the inverse magnetic susceptibility in the temperature region where the diffraction data indicate that devitrification takes place. The data for sample #2 are to be read from the right-hand axis, whereas samples #1 and #3 are to be read from the left-hand axis

was fixed so as to correspond with the H-bonded chains of octahedra, along the *b*-axis in the 9-hydrate and along the *c*-axis in the 8-hydrate. For the supercells described later, we were forced to adopt ferromagnetic structures in order to avoid further increasing the supercell dimensions or further lowering the symmetry since the calculations for the very large low-symmetry spin-polarised supercells are computationally expensive.

Lastly, as is well-known, DFT does not properly treat the Coulomb interactions of highly localised *d* and *f* electrons in transition metal elements (Hubbard 1963). A straightforward correction of the on-site Coulomb interaction (*U*) and the on-site exchange interaction (*J*) to the Hohenberg–Kohn–Sham Hamiltonian is achieved by the use of a Hubbard interaction parameter. The CASTEP implementation adopts the $U_{\text{eff}} = U - J$ approach of Dudarev et al. (1998) and we use a value of $U_{\text{eff}} = 5.96$ eV for Ni taken from Madsen and Novak (2005). Although the value of Hubbard *U* will vary from one compound to another, and indeed from one crystallographic site to another in given material (Cococcioni 2012), we do not expect small deviations to alter the structural parameters in these hydrates significantly. In fact, the very similar degree

of over-binding seen in both $\text{MgSO}_4 \cdot 9\text{H}_2\text{O}$ (where this issue does not occur) and the $\text{NiSO}_4 \cdot 9\text{H}_2\text{O}$ analogue supports this hypothesis. The same value, $U=5.96$ eV, was adopted by Fang et al. (2015) in their recent study of NiSO_4 hydrate, assuring complementarity with this work. The DFT calculation of elastic constants in tetragonal $\text{NiSO}_4 \cdot 6\text{H}_2\text{O}$ (retgersite) did not report the use of a Hubbard correction (Arbeck et al. 2010).

Structural relaxations of the 8- and 9-hydrate under zero-pressure athermal conditions were carried out, starting from the experimental crystal structures [see “Structure determination and completion (8-hydrate)” and “Structure determination and completion (9-hydrate)”), using the BFGS method (Pfrommer et al. 1997). The relaxations were considered to have converged when the forces on each atom were less than 5×10^{-3} eV Å⁻¹ and each component of the stress tensor was smaller than 0.005 GPa. Details of how other specific properties were calculated are given in subsequent sections.

Some additional calculations were done to characterise the solid-solution series $\text{MgSO}_4 \cdot 9\text{H}_2\text{O} - \text{NiSO}_4 \cdot 9\text{H}_2\text{O}$, evaluating the variation in unit-cell parameters and energetic favourability of distributing Ni^{2+} in various ways across the two octahedral sites. The cations occupy two symmetry-inequivalent octahedral sites (Fig. 4), one of which (M1) has a metal-coordinated water molecule that donates a hydrogen bond to the other octahedral site (M2). Hence the difference between the two sites can be simplified to the M1 sites (on Wyckoff positions 2*a*) being “H-bond donors” and the M2 sites (on positions 2*c*) being “H-bond acceptors”.

In addition to the end-member calculations, geometry optimisations were done for compositions corresponding to $(\text{Mg}_{0.5}\text{Ni}_{0.5})\text{SO}_4 \cdot 9\text{H}_2\text{O}$ with Ni^{2+} distributed either entirely on the M1 sites or entirely on the M2 sites. The situation in which Ni^{2+} is evenly distributed between the two sites required the construction of (at least) a $2 \times 1 \times 1$ supercell which, provided the Ni^{2+} is arranged in such a way as to maximise the Ni–Ni distance, retains *P*2₁/c symmetry. In this supercell, the M1 sites are those on Wyckoff positions 2*a* (at 0, 0, 0) and 2*b* (at $\frac{1}{2}, 0, 0$) and the M2 sites are now on positions 2*c* (0, $\frac{1}{2}, 0$) and 2*d* ($\frac{1}{2}, \frac{1}{2}, 0$). The model used to describe the 50:50 distribution of Mg^{2+} and Ni^{2+} is not a particularly good description of the real crystal since it exhibits both short- and long-range order, having a unit cell that would lead to experimentally observable superlattice reflections. However, it is not currently possible to do spin-polarised calculations with partially occupied sites via CASTEP’s Virtual Crystal Approximation.

Results

Structure determination and completion (8-hydrate)

From prior work (Fortes et al. 2012a, b) it was known that $\text{NiSO}_4 \cdot 8\text{H}_2\text{O}$ is triclinic, space-group $P\bar{1}$, with unit-cell

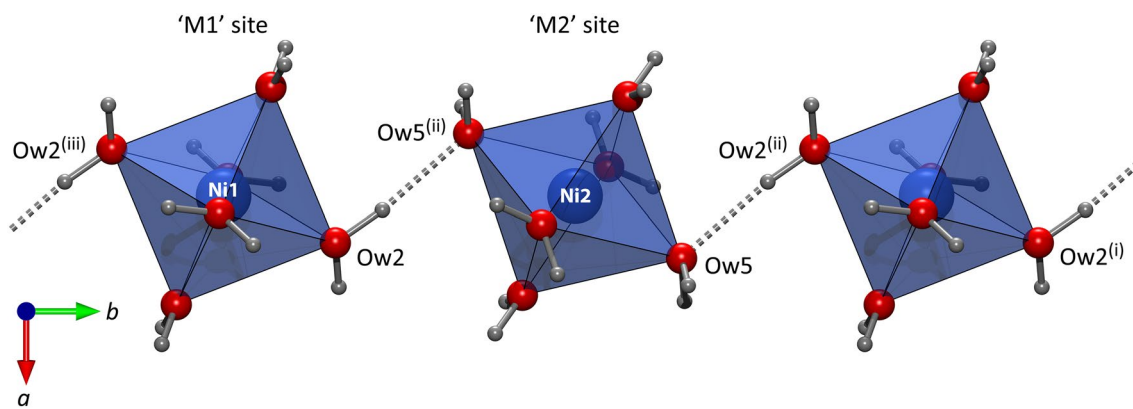


Fig. 4 Illustration of the H-bonded chains of NiO_6 octahedra running along the b -axis in $\text{NiSO}_4 \cdot 9\text{H}_2\text{O}$. Symmetry codes: (i) $x, 1+y, z$; (ii) $-x, 1-y, -z$; (iii) $-x, -y, -z$. Drawn using Diamond (Putz and Brandenburg 2006)

parameters at 260 K $a = 6.13 \text{ \AA}$, $b = 6.86 \text{ \AA}$, $c = 12.63 \text{ \AA}$, $\alpha = 92.9^\circ$, $\beta = 97.7^\circ$, $\gamma = 96.6^\circ$ and $V = 522 \text{ \AA}^3$. Since the packing of the coordination polyhedra is likely, to a first approximation, to be similar to that in other related cryo-hydrates, such as $\text{MgSO}_4 \cdot 9\text{H}_2\text{O}$ and $\text{NiSO}_4 \cdot 9\text{H}_2\text{O}$, a rather obvious trial structure can be generated with $\text{Ni}(\text{H}_2\text{O})_6$ octahedra located on the $1a$ and $1b$ Wyckoff positions $(0, 0, 0)$ and $(0, 0, \frac{1}{2})$. The task of structure solution then reduces to determining the orientation of these octahedra and locating the sulfate tetrahedra [which must be close to $(\frac{1}{2}, \frac{1}{2}, \frac{1}{4})$] using simulated annealing methods, followed by a difference Fourier synthesis to locate the two interstitial water molecules we believe to be present.

The first stage was achieved using the parallel tempering algorithm in FOX, version 1.9.7.1 (Favre-Nicolin and Černý 2002, 2004) starting from the trial structure outlined above. In fact the initial model, including the estimated sulfate oxyanion location, gave fair agreement with the XRD data before running the optimisation. For the 8-hydrate, FOX was used to construct ideal NiO_6 octahedra with $\text{Ni}-\text{O}$ distances of 2.05 \AA , and ideal SO_4 tetrahedra with $\text{S}-\text{O}$ distances of 1.48 \AA ; these were treated as rigid bodies throughout the solution process. In runs of $\frac{1}{2}$ million trials each, the crystal structure was optimised against the X-ray powder diffraction data, consistently producing very similar arrangements of the polyhedra. Importantly, Fourier difference maps phased on these partial structures revealed two well-defined maxima per formula unit that seemed likely to correspond to the additional water molecules necessary to form the expected 8-hydrate. The structure with the lowest overall cost function was exported as a CIF file to form the basis for further analysis.

A set of unique (i.e., ordered) hydrogen atom locations were derived by examination of the nearest neighbours of each non-sulfate oxygen atom, these being positioned 0.98 \AA along the shortest $\text{O}\cdots\text{O}$ vectors. An initial geometry

relaxation of this trial structure in CASTEP then provided the most accurate starting position from which to begin a structural refinement using the experimental data.

The trial structure was refined against both the 260 K X-ray and 150 K neutron powder datasets simultaneously using GSAS/ExpGUI, on the assumption that the atomic fractional coordinates do not vary significantly in this temperature range. The joint refinement takes advantage of the larger coherent scattering cross section of sulfur to X-rays (compared with the equivalent cross section to neutrons) and the large coherent scattering cross section of deuterium to neutrons (with X-rays this is the weakest scatterer) to yield the optimum precision on the positions of all atoms in the crystal. Lattice parameters, phase fractions, background and peak-profile coefficients were allowed to refine independently for the two batches of data (due both to the different instrumental characteristics and the different temperatures), but the shifts in atom-fractional coordinates were constrained to be the same. At the start of the refinement comparatively loose bond distance restraints were applied to the $\text{O}-\text{D}$ contacts ($0.980 \pm 0.005 \text{ \AA}$) but these were switched off in the final cycles of the refinement. Structural parameters are given in Supplementary CIF data and selected bond distances and angles are reported in Table 2 for comparison with the DFT-derived values.

The structure (Fig. 5) consists of isolated $\text{Ni}(\text{H}_2\text{O})_6$ octahedra on sites of $\bar{1}$ symmetry; the $\text{Ni}1$ octahedron, which occupies the $1a$ position, donates a hydrogen bond (via water molecule $\text{Ow}2$) to its neighbouring octahedron, situated on the $1b$ site via water molecule $\text{Ow}5$. This effectively creates H-bonded chains of $\text{Ni}(\text{H}_2\text{O})_6$ octahedra running parallel to the c -axis at $b=0$, which are exactly analogous with the H-bonded chains of octahedra running along the b -axis of the 9-hydrate (cf., Fig. 4). The sulfate tetrahedra occupy channels between the octahedral chains (sitting at $c \approx 0.2$ and $c \approx 0.8$). The two interstitial water molecules, $\text{Ow}7$ and $\text{Ow}8$,

Table 2 Bond lengths and angles in the ionic polyhedra in $\text{NiSO}_4 \cdot 8(\text{H/D})_2\text{O}$ and $\text{NiSO}_4 \cdot 9(\text{H/D})_2\text{O}$ compared with the zero-pressure DFT geometry optimisations

| | | $\text{NiSO}_4 \cdot 9\text{D}_2\text{O}$ (150 K exp) | $\text{NiSO}_4 \cdot 9\text{H}_2\text{O}$ (WC GGA + U) | $\text{NiSO}_4 \cdot 8\text{D}_2\text{O}$ (150 K exp) | $\text{NiSO}_4 \cdot 8\text{H}_2\text{O}$ (WC GGA + U) |
|----------------------|------------------|--|---|--|--|
| <i>a</i> | Å | 6.69737(6) | 6.56234 | 6.1246(1) | 6.17883 |
| <i>b</i> | Å | 11.8627(1) | 11.89859 | 6.8401(1) | 6.79912 |
| <i>c</i> | Å | 14.5668(1) | 14.53436 | 12.5339(2) | 12.34213 |
| α | ° | 90 | 90 | 92.846(1) | 92.35396 |
| β | ° | 94.974(1) | 93.67737 | 97.822(1) | 97.86015 |
| γ | ° | 90 | 90 | 96.627(1) | 96.85721 |
| <i>V</i> | Å ³ | 1152.96(1) | 1132.5434 | 515.58(1) | 509.0855 |
| ΔV | % | – | – 1.77 | – | – 1.26 |
| | % | | – 1.2 | | – 0.7 |
| S–O1 | Å | 1.473(5) | 1.4899 | 1.482(3) | 1.4951 |
| S–O2 ^a | Å | 1.474(5) | 1.4715 | 1.476(2) | 1.4808 |
| S–O3 | Å | 1.482(5) | 1.4956 | 1.480(3) | 1.4942 |
| S–O4 | Å | 1.490(5) | 1.5065 | 1.474(3) | 1.4945 |
| O1–S–O2 | ° | 110.6(4) | 110.35 | 108.9(1) | 109.21 |
| O1–S–O3 | ° | 109.5(4) | 109.22 | 109.5(1) | 109.72 |
| O1–S–O4 | ° | 109.1(4) | 108.98 | 109.7(1) | 108.90 |
| O2–S–O3 | ° | 110.2(4) | 110.15 | 109.3(1) | 109.79 |
| O2–S–O4 | ° | 108.6(4) | 109.48 | 110.0(1) | 110.42 |
| O3–S–O4 | ° | 108.8(4) | 108.63 | 109.4(1) | 108.80 |
| SO_4 volume | Å ³ | 1.662 | 1.7004 | 1.658 | 1.7013 |
| ΔV | % | – | +2.3 | – | +2.6 |
| Ni1–Ow1 | Å | 2.023(6) | 2.0396 | 2.039(2) | 2.0601 |
| Ni1–Ow2 | Å | 2.035(6) | 2.0686 | 2.032(1) | 2.0632 |
| Ni1–Ow3 | Å | 2.046(5) | 2.1093 | 2.074(2) | 2.0807 |
| Ow1–Ni1–Ow2 | ° | 91.3(3) | 91.51 | 90.42(7) | 93.42 |
| Ow1–Ni1–Ow3 | ° | 93.7(2) | 92.92 | 93.09(7) | 91.45 |
| Ow2–Ni1–Ow3 | ° | 90.9(2) | 91.86 | 90.25(6) | 91.51 |
| Ni1 volume | Å ³ | 11.204 | 11.8398 | 11.441 | 11.7634 |
| ΔV | % | – | +5.7 | – | +2.8 |
| Dist index | | 0.0038 | 0.0118 | 0.0083 | 0.0041 |
| Quadr Elong | | 1.0017 | 1.0019 | 1.0011 | 1.0016 |
| Bond angle var | deg ² | 5.9769 | 5.1849 | 3.5536 | 5.8525 |
| Ni2–Ow4 | Å | 2.052(6) | 2.0511 | 2.054(2) | 2.0684 |
| Ni2–Ow5 ^b | Å | 2.089(6) | 2.1087 | 2.040(2) | 2.1350 |
| Ni2–Ow6 | Å | 2.032(5) | 2.0677 | 2.083(1) | 2.0648 |
| Ow4–Ni2–Ow5 | ° | 90.6(3) | 90.84 | 93.94(7) | 93.33 |
| Ow4–Ni2–Ow6 | ° | 90.7(2) | 93.15 | 91.41(7) | 90.81 |
| Ow5–Ni2–Ow6 | ° | 90.5(2) | 90.02 | 91.15(6) | 92.04 |
| Ni2 volume | Å ³ | 11.611 | 11.9054 | 11.603 | 12.1290 |
| ΔV | % | – | +2.5 | – | +4.5 |
| Dist index | | 0.0102 | 0.0106 | 0.0078 | 0.0146 |
| Quadr elong | | 1.0004 | 1.0013 | 1.0020 | 1.0021 |
| Bond angle var | deg ² | 0.3868 | 3.8572 | 6.8556 | 5.7789 |

The octahedral distortion index, quadratic elongation (λ_{oct}) and bond-angle variance (σ_{oct}^2) are defined by Robinson et al. (1971) and calculated using VESTA (Momma and Izumi 2011)

^aAccepts two H-bonds (all others accept three)

^bH-bond acceptor in tetrahedral coordination

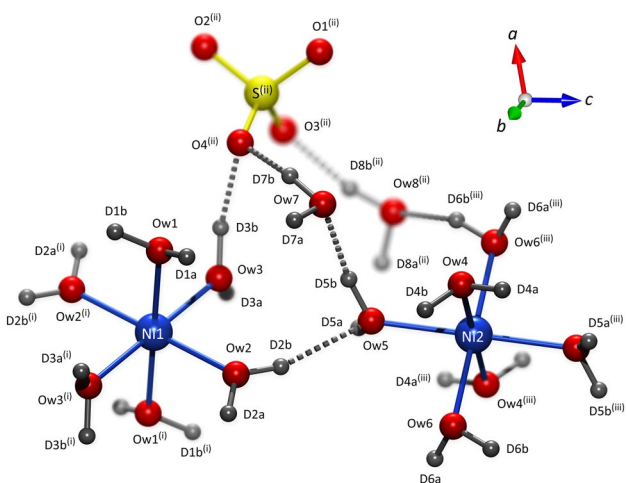


Fig. 5 The asymmetric unit of $\text{NiSO}_4 \cdot 8\text{H}_2\text{O}$ and such other atoms as are necessary to complete the polyhedral representation. Symmetry codes: (i) $-x, -y, -z$; (ii) $x, y-1, z$; (iii) $-x, -y, 1-z$

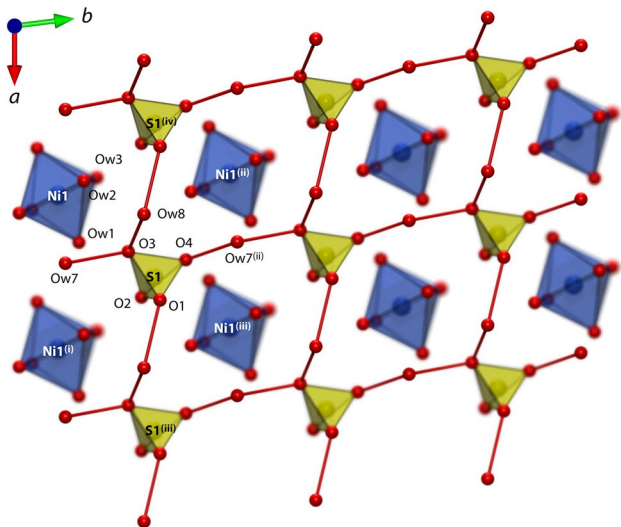


Fig. 6 Depiction of the network formed by the hydrogen bonding between the interstitial water molecules and the sulfate tetrahedra in $\text{NiSO}_4 \cdot 8\text{H}_2\text{O}$. Symmetry codes: (i) $x+1, y, z$; (ii) $x, y+1, z$; (iii) $x+1, y+1, z$; (iv) $x-1, y, z$

donate hydrogen bonds to the apical sulfate oxygens O3 and O4 to create a reticular motif in the $a-b$ plane. The relationship between this sulfate–water net and the sulfate–water pentagonal ribbons in the 9-hydrate is shown in Fig. 6.

The sulfate oxygens O1, O3 and O4 each accept three hydrogen bonds whilst O2 accepts only two. The effect of this is typically manifested in the S–O bond lengths, those with the least number of H-bond connections tending to have the shortest S–O length. Whilst this is evident from the DFT calculations (Table 2), the differences in S–O bond lengths obtained experimentally show no such systematic variation.

The agreement between the DFT geometry optimisation (0 K) and the experimental structure refinement (150 K) is good. Only the calculated c -axis length differs from the experimental value by more than 1% and the overall difference in unit-cell volume is 1.3%. The DFT + U calculations yield S–O and Ni–O distances that are longer than the experimental values and so the polyhedral volumes are too great by 3–5%. This is not a deficiency of the spin-polarised calculations or the adopted value of U_{eff} , since the same differences were observed in $\text{MgSO}_4 \cdot 9\text{H}_2\text{O}$ (Fortes et al. 2017b). Further comparisons will be made in the context of the 9-hydrate structure in the following section.

Structure determination and completion (9-hydrate)

The structure of $\text{NiSO}_4 \cdot 9\text{D}_2\text{O}$ was refined using neutron powder diffraction data collected at 150 K using the published structure of the Mg-bearing analogue as a starting point. As with the octahydrate, bond distance restraints were applied in the early cycles of refinement and were subsequently turned off. Structural parameters are given in Supplementary CIF data and selected bond distances and angles are reported in Table 2 for comparison with the DFT-derived values. Since the structure is isotopic with $\text{MgSO}_4 \cdot 9\text{D}_2\text{O}$, readers are referred to Fortes et al. (2017b) for a description of how the coordination polyhedra and interstitial water molecules are arranged. The following discussion will focus on comparisons with calculations and differences with the Mg analogue and with NiSO_4 octahydrate.

The sulfate tetrahedra in $\text{NiSO}_4 \cdot 9\text{D}_2\text{O}$, $\text{NiSO}_4 \cdot 8\text{D}_2\text{O}$ and $\text{MgSO}_4 \cdot 9\text{D}_2\text{O}$ are identical (within errors) in volume, since each accepts the same overall number of hydrogen bonds. The M^{2+}O_6 octahedra in the NiSO_4 cryohydrates are slightly smaller in volume than in the MgSO_4 analogue, but the deviations from perfectly regular octahedral geometry are very similar. In the two 9-hydrates, the M1 octahedral site is smaller than the M2 site and exhibits a larger bond-angle variance; this is reproduced in the DFT calculations for both the Mg and Ni species. Equally, the M2 site is elongated along the $\text{M}^{2+}\text{–Ow5}$ axis (the H-bond acceptor) in both Mg and Ni species, whereas the M1 site is elongated along the $\text{M}^{2+}\text{–Ow3}$ axis (perpendicular to the H-bond donor, Ow2). The signature of this is not clear in the $\text{NiSO}_4 \cdot 9\text{D}_2\text{O}$ structure refinement, but is present in the experimental $\text{MgSO}_4 \cdot 9\text{D}_2\text{O}$ refinement and in the $\text{NiSO}_4 \cdot 8\text{D}_2\text{O}$ structure as well as in all of the calculations.

The main structural elements and the overall packing of the 8-hydrate are thus found to be very similar indeed to the 9-hydrate.

Magnetic property measurements

The inverse molar susceptibility of a $\text{NiSO}_4 \cdot 9\text{H}_2\text{O} + \text{ice Ih}$ mixture over the range 2–240 K is shown in Fig. 7. At high temperatures the material exhibits the expected Curie–Weiss behaviour for a paramagnetic material with no evidence of magnetic ordering at lower temperatures; only the anomalous deviation due to devitrification at 225 K departs from this behaviour. Six separate data segments measured between 175 and 240 K in three different samples were fitted with a linear relation, $1/\chi_m = (T - \theta)/C$, where θ is the Weiss constant and C is the Curie constant. From these, we obtain mean values and standard deviations of the fit parameters, $\theta = 13(3)$ K and $C = 1.10(2) \text{ emu}^{-1} \text{ mol Oe K}^{-1}$. The latter is used to obtain the moment on the Ni^{2+} ion, $3.1(1) \mu_B$, which is slightly larger than the spin-only value ($2.83 \mu_B$) and likely reflects an orbital contribution to the observed moment.

The positive value of the Weiss constant is indicative of ferromagnetic coupling between neighbouring Ni^{2+} ions. Since the ions are coordinated by water, the interaction between them must inevitably be mediated through the hydrogen bond network. The $\text{Ni}(\text{H}_2\text{O})_6$ octahedra are directly linked through $\text{Ow}2-\text{H}2\text{a}\cdots\text{Ow}5$ to form 1D chains, so the most direct exchange pathway is across this hydrogen bridge. There are comparatively few examples in the literature of super-exchange coupling via hydrogen bonds. However, the available experimental and computational evidence points in general to weak antiferromagnetic coupling when the H-bonds are short, $\text{O}\cdots\text{O} \approx 2.4 \text{ \AA}$, becoming progressively weaker or becoming ferromagnetic for longer H-bonds, $\text{O}\cdots\text{O} > 2.8 \text{ \AA}$ (Desplanches et al. 2002; Ma et al.

2010; Bandeira and Le Guennic 2012; Cortijo et al. 2013). In $\text{NiSO}_4 \cdot 9\text{H}_2\text{O}$ the $\text{O}\cdots\text{O}$ separation is 2.985 \AA , so it is not too surprising that we should find evidence of ferromagnetic coupling.

Watanabe (1962) measured the magnetic susceptibility of single-crystal and powder samples of $\text{NiSO}_4 \cdot 7\text{H}_2\text{O}$ and the tetragonal polymorph of $\text{NiSO}_4 \cdot 6\text{H}_2\text{O}$. For comparison with our work, Watanabe reported $\theta_{\text{powder}} = -0.3 \text{ K}$ for the heptahydrate and $+0.4 \text{ K}$ for the hexahydrate. In both of these salts there are also direct H-bonds between the $\text{Ni}(\text{H}_2\text{O})_6$ coordination polyhedra, with $\text{O}\cdots\text{O}$ separations of 2.864 \AA in $\text{NiSO}_4 \cdot 7\text{H}_2\text{O}$ (Ptasiewicz-Bak et al. 1997) and 2.790 \AA in $\text{NiSO}_4 \cdot 6\text{H}_2\text{O}$ (Angel and Finger 1988). These are both substantially shorter than the interpolyhedral H-bond in $\text{NiSO}_4 \cdot 9\text{H}_2\text{O}$, which may explain both the difference in magnitude and sign of the Weiss constant for the two lower hydrates. None of the hydrates with $6 < n < 7$ exhibit any evidence of magnetic ordering at low temperature (Fisher et al. 1967, 1968a, b; Fisher and Hornung 1968; Stout and Hadley 1964; Stout et al. 1966), by contrast with anhydrous NiSO_4 which contains antiferromagnetic sheets with ferromagnetic coupling between the sheets (Frazer and Brown 1962).

DFT calculations reveal no significant difference in the total energy or lattice parameters for ferromagnetic or anti-ferromagnetic spin configurations in either $\text{NiSO}_4 \cdot 8\text{H}_2\text{O}$ or $\text{NiSO}_4 \cdot 9\text{H}_2\text{O}$ (Table 3). The calculated band gaps in the octahydrate and enneahydrate are 3.862 and 3.794 eV , respectively. For comparison with other work, we carried out a geometry relaxation and band structure calculation on $\text{NiSO}_4 \cdot 7\text{H}_2\text{O}$, finding a band gap of 4.005 eV . This is lower than the value of Fang et al. (2015), who reported a band gap of 5.24 eV for the heptahydrate and $5.14/5.05 \text{ eV}$ for the monoclinic/tetragonal polymorphs of the hexahydrate.

Behaviour on warming

The range of existence of the two new hydrates is comparatively small. The enneahydrate forms at 220 K on devitrification of the flash-frozen brine, and then exsolves one water molecule per formula unit between 245 and 250 K to form $\text{NiSO}_4 \cdot 8\text{H}_2\text{O} + \text{ice Ih}$ (Fig. 8). The octahydrate is itself unstable with respect to the heptahydrate and a slow progressive solid-state transformation of $\text{NiSO}_4 \cdot 8\text{H}_2\text{O}$ to $\text{NiSO}_4 \cdot 7\text{H}_2\text{O} + \text{ice Ih}$ occurs on warming above 250 K. A sudden change of all residual octahydrate to heptahydrate is then observed between 272 and 274 K, followed shortly afterwards by the onset of eutectic melting at $\sim 276 \text{ K}$. The behaviour of $\text{NiSO}_4 \cdot 7\text{H}_2\text{O}$ at higher temperatures has been described elsewhere (Maneva et al. 1990).

These data correspond with the pure end-member nickel sulfate. Our previous work, done with a small Peltier-cooled X-ray stage, allowed us to achieve temperatures of $\sim 255 \text{ K}$ and we observed the octahydrate only in 90–100 atom % Ni

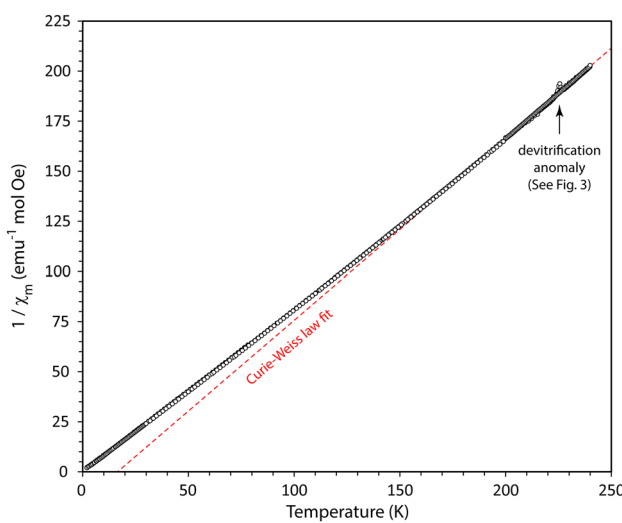


Fig. 7 Inverse molar susceptibility ($\text{emu}^{-1} \text{ mol Oe}$) of the $\text{NiSO}_4 \cdot 9\text{H}_2\text{O} + \text{ice Ih}$ mixture as a function of temperature. The dashed red line represents a linear fit to the high-temperature data, following the Curie–Weiss law. The small anomaly highlighted at $\sim 220 \text{ K}$ is shown in greater detail in Fig. 3

Table 3 Unit-cell parameters and total electronic energy for the two NiSO_4 hydrates modelled with different spin configurations

| | $\text{NiSO}_4 \cdot 8\text{H}_2\text{O}$ | | $\text{NiSO}_4 \cdot 9\text{H}_2\text{O}$ | |
|-----------------------|---|-------------------------|---|-------------------------|
| | FM (001) M1 ↑, M2 ↑ | AFM (001) M1 ↑, M2 ↓ | FM (010) M1 ↑, M2 ↑ | AFM (010) M1 ↑, M2 ↓ |
| a (Å) | 6.180342 | 6.180319 | 6.562337 | 6.562337 |
| b (Å) | 6.800725 | 6.800170 | 11.898592 | 11.898592 |
| c (Å) | 12.353434 | 12.353965 | 14.534360 | 14.534360 |
| α (°) | 92.363363 | 92.378918 | 90 | 90 |
| β (°) | 97.868837 | 97.872989 | 93.677371 | 93.677371 |
| γ (°) | 96.862300 | 96.873497 | 90 | 90 |
| V (Å ³) | 509.774819 | 509.726720 | 1132.543418 | 1132.543421 |
| E (eV) | – 14239.7561442 | – 14239.7561733 | – 30353.4845366 | – 30353.4843091 |

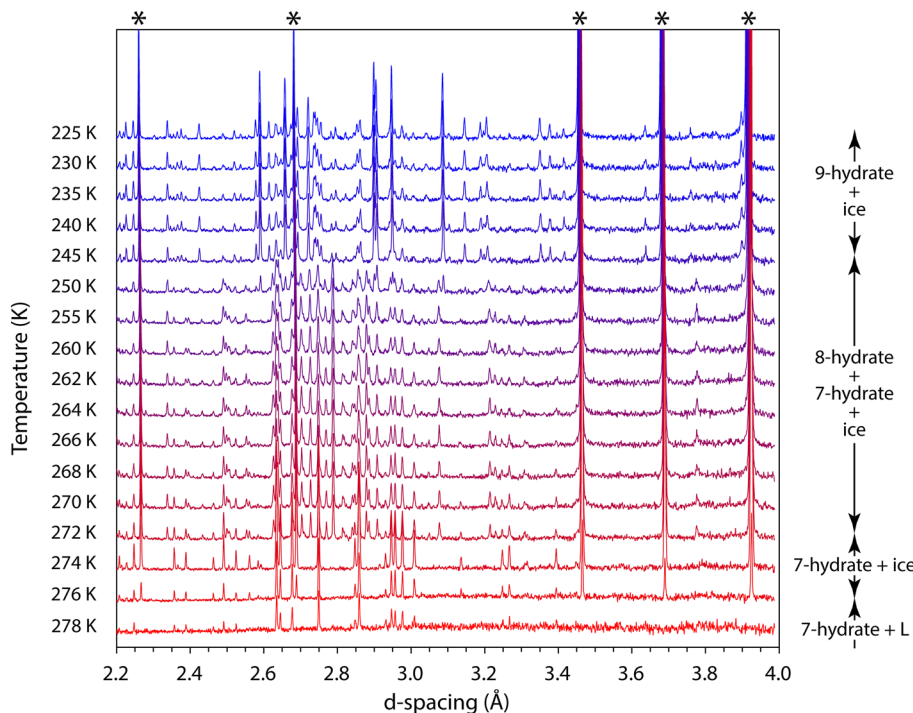
samples at this temperature; lower concentrations of Ni^{2+} (between 40 and 90 atom %) resulted in the formation of the enneahydrate. In terms of the thermal stability, $\text{NiSO}_4 \cdot 9\text{H}_2\text{O}$ containing 10–60 atom % Mg is able to persist to at least 255 K, whereas more nickel-rich compositions are unstable and we observe the octahydrate instead at this temperature. The implication of this is that the temperature at which the enneahydrate breaks down to the octahydrate decreases with increasing nickel content. Further temperature-dependent studies on a range of compositions are required to establish this with certainty.

(Mg,Ni)SO₄·9H₂O solid solutions

It was noted previously (Fortes et al. 2017b, their Supplementary Figure S2) that X-ray powder diffraction

measurements on (Mg, Ni)SO₄·9H₂O solid solutions indicated some degree of site ordering in the crystal. All but three of our neutron powder datasets are suitable for refinement of site occupancies. Since these data are multiphase and dominated at short d-spacings by ice Bragg peaks, the accuracy of the site occupancies is limited but we nonetheless find that there is indeed a marked preference for Ni^{2+} to substitute for Mg^{2+} on the 2c sites at (0, 0, ½), as shown in Fig. 9; whilst these M2 octahedra are marginally larger than the M1 octahedral sites (by ~3%) they are considerably less distorted, indicating that crystal field stabilisation energy rather than cation radius is the main factor in determining the site substitution preference. This seems remarkable given the rather extreme disequilibrium nature of the synthesis and the improbability of achieving any intersite diffusional equilibrium at 150–200 K. Fitting a simple quadratic expression

Fig. 8 Neutron powder diffraction patterns collected on warming between 225 and 278 K showing the sequence of transitions from $\text{NiSO}_4 \cdot 9\text{H}_2\text{O} \rightarrow \text{NiSO}_4 \cdot 8\text{H}_2\text{O} \rightarrow \text{NiSO}_4 \cdot 7\text{H}_2\text{O}$. The strongest Bragg peaks from water ice are marked near the top by asterisks; note that ice is not present in the last dataset at 278 K indicative of warming above the eutectic



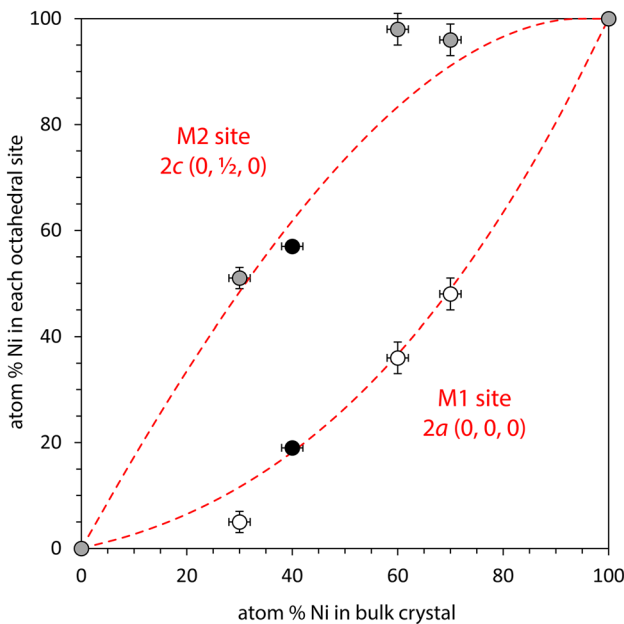


Fig. 9 Partitioning of Ni^{2+} between the two available sites in the $(\text{Mg},\text{Ni})\text{SO}_4 \cdot 9\text{H}_2\text{O}$ structure. Open grey and white symbols show the distribution of Ni^{2+} into the M1 and M2 sites as determined by refinement of neutron powder diffraction data collected from octahydrate-free specimens. The filled black symbols show the distribution obtained by refinement of a high-quality X-ray powder diffraction dataset on $(\text{Mg},\text{Ni})\text{SO}_4 \cdot 9\text{H}_2\text{O}$

between the two end-member compositions (dashed lines in Fig. 9) gives a slowly varying site-distribution coefficient, $K_D = [(\text{Ni}/\text{Mg})_{(2a)}]/[(\text{Ni}/\text{Mg})_{(2c)}]$ with a mean value of 7.6(6) from 0 to 60 atom % Ni^{2+} ; the minimum $K_D = 7.1$ occurs near 30 atom % Ni^{2+} and increases substantially at higher concentrations.

These values are closely comparable to the case of Ni^{2+} substitution in Mg_2SiO_4 olivine, where Ni^{2+} prefers the smaller and more distorted M1 site, with minimum K_D values in the region of 6–10 at intermediate compositions and higher values towards the Mg- or Ni-rich end-members (Rajamani et al. 1975; Bish 1981; Boström 1987; Ottonegro et al. 1989; Tsukimura and Sasaki 2000; Henderson et al. 2001). Of itself, site ordering is not necessarily indicative of thermodynamically non-ideal solution behaviour. However, there is a small but significant positive excess volume of mixing manifested in the unit-cell refinements (Fig. 10; Table 4); this deviation from a linear relationship between the volumes of the end-members (Retger's “law”) is indicative of a non-ideal solid solution.

Each of the cell parameters given in Table 4 has been fitted with an equation that describes the deviation from linearity (aka Vegard's “law”) using a quadratic expression:

$$a = a_{\text{Mg}}^0 (1 - X) + a_{\text{Ni}}^0 (X) + \delta' X(1 - X)^2 + \delta'' (1 - X)X^2, \quad (1)$$

where a_{Mg}^0 and a_{Ni}^0 are the cell parameters of the end-members, X is the Ni atom fraction and δ' and δ'' characterise the deviation from linearity. Parameters from these fits are reported in Table 5 and are shown as solid lines in Fig. 10. The main contributor to the positive volume excess comes from the b -axis, which exhibits a substantial and asymmetric deviation from linearity as a function of composition, reaching a maximum of ~0.15% at 40 atom % Ni^{2+} . Conversely, the a -axis exhibits a negative deviation from Vegard's law whilst both c and β display trends that are statistically indistinguishable from linear. The extent to which this behaviour mimics the observations of Ni-doped olivine is remarkable. With replacement of Mg^{2+} by Ni^{2+} in olivine, the crystal's b -axis displays an initial plateau or convex upward trend followed by a sharp decrease, exactly as seen in $\text{MgSO}_4 \cdot 9\text{H}_2\text{O}$, whereas the a - and c -axes show very slight negative deviations from linearity (Matsui and Syono 1968; Rajamani 1975; Boström 1987; Vokurka and Rieder 1987; Hirschmann 1992; Chen et al. 1996; Henderson et al. 2001).

The model fits to the lattice parameters are used to determine the infinitesimal elastic strain tensor due to ionic substitution (e.g., Hazen et al. 2000); Fig. 11a shows a series of representations of the strain tensor (cf., Hashash et al. 2003). The eigenvalues and eigenvectors of these strain tensors, obtained by standard matrix decomposition methods, are the magnitudes and orientations of the principal strain directions (Fig. 11b).

As expected, the main feature is a systematic increase in the magnitude of the negative strain parallel with the b -axis (ε_2), corresponding to shortening of the H-bonded octahedral chains due to substitution of Mg^{2+} with the smaller Ni^{2+} cation (Shannon 1976). Although ε_1 and ε_3 do not vary so substantially, there is large rotation of the strain tensor such that the angle between ε_1 and the c -axis changes from 66° to 23° . What this shows is that at low Ni dopant concentrations in $\text{MgSO}_4 \cdot 9\text{H}_2\text{O}$, the largest contraction is in the spacing between adjacent H-bonded octahedral chains (i.e., roughly along the a -axis); at intermediate concentrations, shortening of these chains becomes prevalent; at high concentration, shortening of the gap between the sheets of octahedral chains is of a similar magnitude to that along the length of the chains.

Calculations of the strain due to substitution of Ni into the structure of $\text{MgSO}_4 \cdot 9\text{H}_2\text{O}$, with the Ni distributed in various ways across the two available sites, produces good qualitative agreement with the observations. The absolute magnitudes of the distortions are much larger than observed experimentally, but the signs and relative magnitudes agree quite well.

For the a -axis, substituting Ni onto the M1 site produces a large positive deviation from Vegard's law whilst substitution of Ni onto M2 results in a small negative deviation.

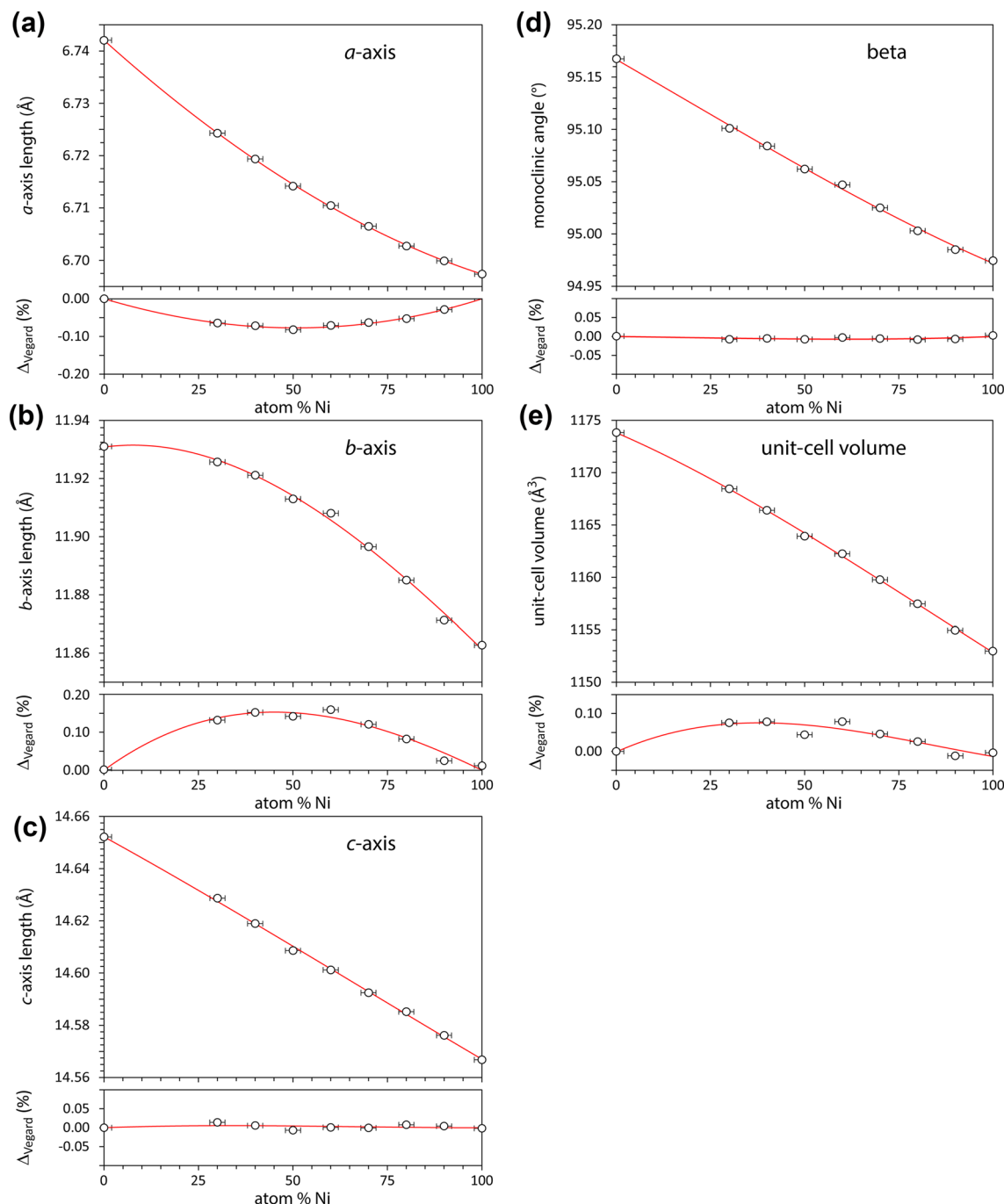


Fig. 10 Unit cell parameters of $(\text{Mg},\text{Ni})\text{SO}_4 \cdot 9\text{D}_2\text{O}$ as a function Ni^{2+} dopant concentration (atom %) at 150 K. Solid lines are least-squares fits of Eq. (1); the plots underneath each parameter report the relative

difference between the observed/model cell parameters and a linear mixing model (i.e., Vegard's/Retger's "law")

For the b -axis, we observe the reverse; substitution of Ni onto M1 produces a negative deviation from Vegard's law, whereas substitution onto the M2 site generates a large positive deviation. For the c -axis, the deviation from Vegard's law produced by substitution of Ni is very small indeed (approximately ten times smaller than the maximum deviation in the b -axis) and does not vary at all according to the

site preference of the cations. Similarly for β , the deviation is small (~one-half that of the c -axis) but is slightly positive for Ni situated on M1 and slightly negative for Ni located on M2.

Using the geometry relaxations from the DFT calculations done for three different nickel distributions, we can obtain a rough estimate of the magnitude of the deviations

Table 4 Cell parameters from neutron powder diffraction analysis of the $\text{MgSO}_4\cdot 9\text{D}_2\text{O}$ – $\text{NiSO}_4\cdot 9\text{D}_2\text{O}$ solid-solution series as a function of nickel content

| Atom % Ni | a (Å) | b (Å) | c (Å) | β (°) | V (Å 3) |
|-----------|------------|------------|------------|-------------|---------------|
| 30 | 6.72430(9) | 11.9257(2) | 14.6287(2) | 95.101(1) | 1168.46(2) |
| 40 | 6.7194(1) | 11.9211(2) | 14.6190(3) | 95.084(2) | 1166.41(3) |
| 50 | 6.7142(2) | 11.9130(3) | 14.6086(4) | 95.062(2) | 1163.92(4) |
| 60 | 6.71047(9) | 11.9081(2) | 14.6012(2) | 95.047(1) | 1162.24(2) |
| 70 | 6.70652(8) | 11.8965(1) | 14.5925(2) | 95.025(1) | 1159.78(2) |
| 80 | 6.7028(1) | 11.8850(2) | 14.5852(3) | 95.003(2) | 1157.46(3) |
| 90 | 6.69989(7) | 11.8712(1) | 14.5761(2) | 94.985(1) | 1154.94(2) |
| 100 | 6.69737(6) | 11.8627(1) | 14.5668(1) | 94.974(1) | 1152.96(1) |

Table 5 Parameters obtained by fitting of Eq. (1) to unit-cell parameters of $(\text{Mg}, \text{Ni})\text{SO}_4\cdot 9\text{D}_2\text{O}$ as a function of Ni content

| a -axis | b -axis | c -axis | β | Volume |
|-------------------|-----------|-----------|------------|-----------|
| x_{Mg}^0 | 6.7420(2) | 11.931(1) | 14.6522(8) | 95.167(2) |
| x_{Ni}^0 | 6.6974(2) | 11.861(1) | 14.5670(5) | 94.972(2) |
| δ' | −0.020(1) | 0.09(1) | 0.005(5) | −0.03(2) |
| δ'' | −0.021(1) | 0.06(1) | − | 5.378 |
| | | | | 1.851 |

corresponding with the experimentally observed case of 75% of the Ni ions being located on the M2 site. In this circumstance, the maximum deviations from linearity in the a - and b -axis are −0.19 and +0.43, respectively, compared with −0.08 and +0.15 observed experimentally. Hence the signs are correct, but the calculated magnitudes are too large by a factor of ~2–3. For the c -axis and for β , the DFT-calculated deviations from linearity are +0.08 and −0.05, respectively, compared with +0.01 and −0.01 experimentally. For the

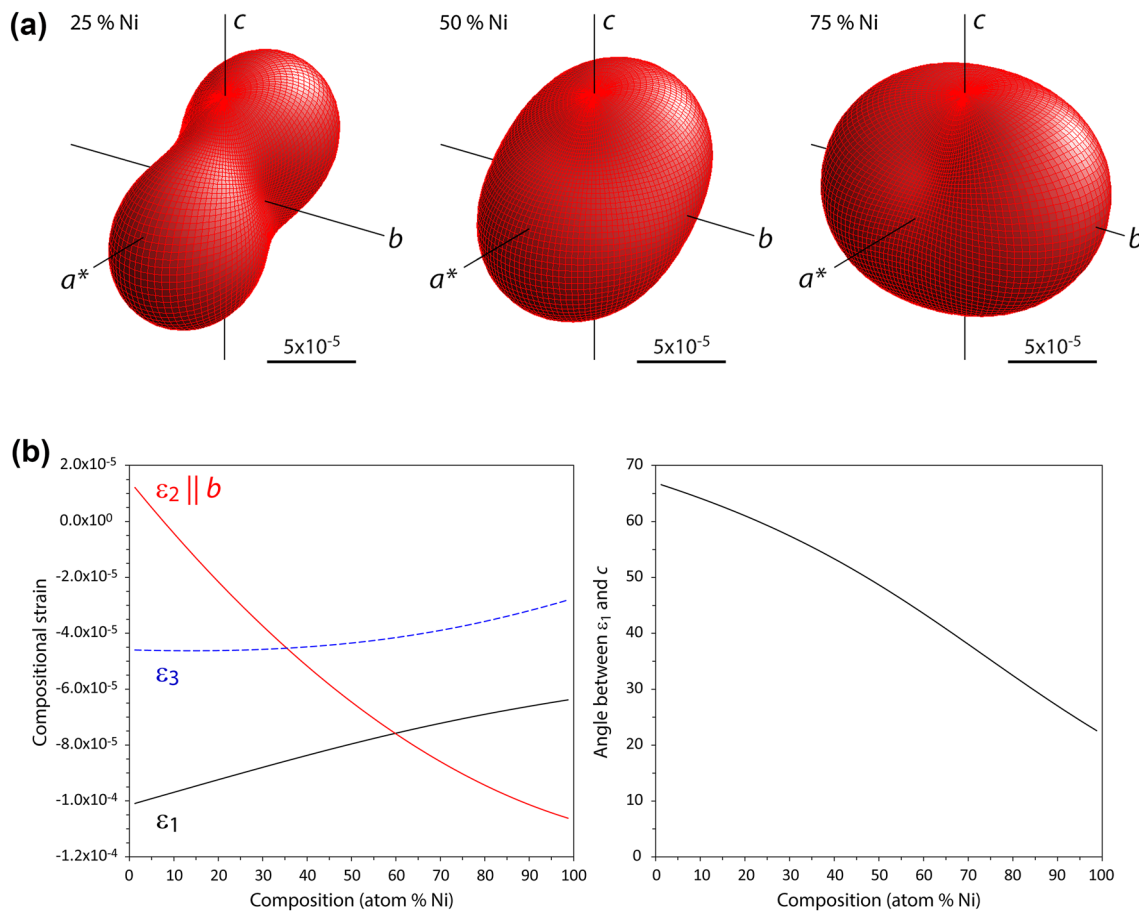


Fig. 11 **a** Tensor representation of the substitutionally induced strain in $(\text{Mg}, \text{Ni})\text{SO}_4\cdot 9\text{D}_2\text{O}$ derived from the lattice parameters in Table 4. Drawn using WinTensor (Kaminski 2004). **b** Variation of the magni-

tude of the principal strains, and the angle between ε_1 and the c -axis, with composition

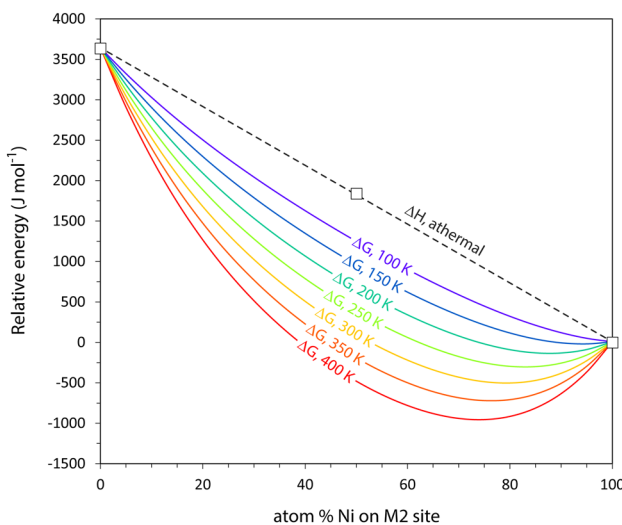


Fig. 12 Variation of Gibbs free energy as a function of the distribution of nickel between the M1 and M2 sites in $\text{NiSO}_4 \cdot 9\text{H}_2\text{O}$. The open squares are the results of athermal DFT+U calculations and the dashed line depicts a linear variation through these points. Accounting for configurational entropy (Eqs. 2, 3) at higher temperatures results in the coloured curves

unit-cell volume, the calculated deviation from Vegard's law is +0.32, whereas the experimental value is +0.08.

Overall, both the experimental and computational view is that the deviations from Vegard's law produced by nickel substitution are confined entirely to the *a*-*b* plane, this being parallel with the octahedral sheets in the structure, with the largest effect being along the *b*-axis, the direction in which the octahedra are most directly connected by the Ow2–H2a...Ow5 hydrogen bond. It seems remarkable that distribution of dopants in these H-bonded octahedral chains should have such a dramatic effect: a crystal containing 50 atom % Ni where all of the Ni ions are on M1 has a *b*-axis that is 0.16 Å (1.3%) shorter than a crystal where those 50% of Ni ions are all on the M2 site. Whilst this may not appear to be a large reduction, it is more than twice as big as the change in the *b*-axis length in $\text{MgSO}_4 \cdot 9\text{D}_2\text{O}$ on cooling from 260 to 10 K and it is roughly equivalent to the change in *b*-axis length caused by the application of 600 MPa of hydrostatic pressure (Fortes et al. 2017b).

As noted earlier, the model used to describe the 50:50 distribution of Mg^{2+} and Ni^{2+} is not a very good analogue of the real crystal. Site disorder in the real crystal will act to dilute the effect of having Ni^{2+} located wholly on the M1 or M2 sites, reducing the deviations from Vegard's law and providing a possible explanation for the difference between the experimental and computational lattice parameters as a function of composition.

DFT calculations also allow us to evaluate the relative energetic stability of the various ion configurations. As shown in Fig. 12, the configuration in which all Ni occupies

the M1 site has an enthalpy (in the athermal limit) that is 3643.4 J mol⁻¹ higher than the configuration where all Ni occupies the M2 site. The calculated enthalpy of the configuration in which the Ni ions are equally distributed over both sites has an enthalpy 1840.06 J mol⁻¹ above the “all M2” reference state. Hence, in the athermal limit the variation is linear.

The effect of temperature is considered by calculation of the configurational entropy. For a two-site lattice, the configurational entropy, S_{conf} is related to the site occupancies by:

$$S_{\text{conf}} = -R \left(v_{\text{M1}} \sum x_i^{\text{M1}} \ln x_i^{\text{M1}} \right) - R \left(v_{\text{M2}} \sum x_i^{\text{M2}} \ln x_i^{\text{M2}} \right), \quad (2)$$

where v_{M1} and v_{M2} are the number of moles of M1 and M2 sites per formula unit and x_i^{M1} , for example, is the fractional occupancy of species i on the M1 site. For the case of site ordering, where $x_{\text{Ni}}^{\text{M1}} = 1$, $x_{\text{Ni}}^{\text{M2}} = 0$, and site anti-ordering, where $x_{\text{Ni}}^{\text{M1}} = 0$, $x_{\text{Ni}}^{\text{M2}} = 1$, the total configurational entropy is zero. For the case of complete disorder across the two sites, S_{conf} reaches a minimum value of $5.762 \text{ J K}^{-1} \text{ mol}^{-1}$. The difference in free energy, ΔG , from the site anti-ordered crystal is:

$$\Delta G = \Delta H - T \Delta S_{\text{conf}}. \quad (3)$$

Figure 12 shows the variations in ΔG for a range of temperatures; the energy minimum at 250 K corresponds to a distribution of ~83:17 for Ni on the M2:M1 sites, which agrees very well with the observed 75:25 distribution, despite the apparent lack of opportunity for equilibrium to be reached during the quench synthesis of our specimens. The substantial energetic preference for Ni to occupy the M2 is matched in similar calculations on both Zn- and Fe-doped analogues. For Fe^{2+} the athermal energy difference between M1 and M2 sites is considerably larger than the Ni species (7442.6 J mol⁻¹) and for Zn^{2+} it is somewhat smaller (2745.0 J mol⁻¹).

Concluding remarks

We have determined the structure of $\text{NiSO}_4 \cdot 8\text{D}_2\text{O}$ for the first time, including all hydrogen atom positions, using a combination of X-ray and neutron powder diffraction and we have refined the structure of $\text{NiSO}_4 \cdot 9\text{D}_2\text{O}$ using neutron powder data. Both contain virtually identical chains of directly H-bonded NiO_6 octahedra although other aspects of their framework (by virtue of the different number of interstitial water molecules) are not the same. Neither crystal is stable in aqueous solution, undergoing subsolidus transformations to the heptahydrate (morenosite) + ice prior to eutectic melting. Experimentally, there is evidence for weak ferromagnetic coupling in $\text{NiSO}_4 \cdot 9\text{H}_2\text{O}$

even though calculations show no differences in energy or structure for different spin configurations.

Isotypic enneahydrates of Mg-, Zn-, Fe- and Ni-sulfates have now been produced synthetically and may occur naturally in environments where aqueous solutions containing these solutes are frozen very quickly, such as in cryovolcanic vents on the surfaces of icy planetary bodies. Annealing between 250 and 270 K should also result in the formation of NiSO_4 octahydrate in these environments. Further work to characterise the vibrational spectra of these materials is required to aid their detection by remote sensing in such localities.

Acknowledgements The authors thank the STFC ISIS facility for beam-time as well as access to the SCARF scientific computing cluster and thank ISIS Technical Support staff for their assistance both on the beamline and in the Materials Characterisation Laboratory. ADF and IGW acknowledge funding from the UK Science and Technology Facilities Council (STFC), Grant numbers PP/E006515/1 and ST/K000934/1.

Open Access This article is distributed under the terms of the Creative Commons Attribution 4.0 International License (<http://creativecommons.org/licenses/by/4.0/>), which permits unrestricted use, distribution, and reproduction in any medium, provided you give appropriate credit to the original author(s) and the source, provide a link to the Creative Commons license, and indicate if changes were made.

References

- Angel RJ, Finger LW (1988) Polymorphism of nickel sulfate hexahydrate. *Acta Cryst C* 44:1869–1873
- Arbeck D, Haussühl E, Bayarjagal L, Winkler B, Paulsen N, Haussühl S, Milman V (2010) Piezoelastic properties of retgersite determined by ultrasonic measurements. *Eur Phys J B* 73:167–175
- Bain GA, Berry JF (2008) Diamagnetic corrections and Pascal's constants. *J Chem Ed* 85:532–536
- Bandeira NAG, Le Guennic B (2012) Calculation of magnetic couplings in hydrogen-bonded Cu(II) complexes using density functional theory. *J Phys Chem A* 116:3465–3473
- Belozerov AS, Anisimov VI (2014) Coulomb interaction parameters in bcc iron: an LDA + DMFT study. *J Phys C Condens Matter* 26:375601
- Benrath A, Schröder W (1927) Über das octahydrat des magnesium-sulfats. *Z Anorg Allg Chem* 161:155–158
- Bish DL (1981) Cation ordering in synthetic and natural Ni–Mg olivine. *Am Mineral* 66: 770–776
- Boström D (1987) Single-crystal X-ray diffraction studies of synthetic Ni–Mg olivine solid solutions. *Am Mineral* 72: 965–972
- Chen J, Li R, Parise JB, Weidner DJ (1996) Pressure-induced ordering in $(\text{Ni}, \text{Mg})_2\text{SiO}_4$ olivine. *Am Mineral* 81: 1519–1522
- Chrétien A, Rohmer R (1934) Sur les hydrates du sulfate de nickel. *CR Hebd Acad Sci* 198: 92–94
- Clark SJ, Segall MD, Pickard CJ, Hasnip PJ, Probert MJ, Refson K, Payne MC (2005) First principles methods using CASTEP. *Z Krist* 220:567–570
- Coccioni M (2012) The LDA + U approach: a simple Hubbard correction for correlated ground states. In: Pavarini E, Koch E, Anders F, Jarrell M (eds) Correlated electrons: from models to materials. Modeling and simulation, vol 2. Forschungszentrum Julich, Julich
- Cortijo M, González-Prieto R, Herrero S, Jiménez-Aparicio R, Sánchez-Rivera P (2013) Ferromagnetic interactions through hydrogen bonds in a one-dimensional Ni(II) coordination polymer. *Eur J Inorg Chem* 2013:5523–5527
- D'Ans J (1933) Die Lösungsgleichgewichte der System der Salz ozeanischer Salzablagerungen. Springer, Berlin, pp 118–123
- Desplanches C, Ruiz E, Rodríguez-Fortea A, Alvarez S (2002) Exchange coupling of transition-metal ions through hydrogen bonding: a theoretical investigation. *J Am Chem Soc* 124:5197–5205
- Dudarev SL, Botton GA, Savrasov SY, Humphreys CJ, Sutton AP (1998) Electron-energy-loss spectra and the structural stability of nickel oxide: an LSDA + U study. *Phys Rev B* 57:1505–1509
- Fang C, Lu X, Buijs W, Fan Z, Genceli-Güner FE, van Huis MA, Witkamp GJ, Vlugt TJH (2015) Crystal structure, stability, and electronic properties of hydrated metal sulfates $\text{MSO}_4(\text{H}_2\text{O})_n$ ($\text{M} = \text{Ni}, \text{Mg}; n = 6, 7$) and their mixed phases: a first principles study. *Chem Eng Sci* 121:77–86
- Favre-Nicolin V, Černý R (2002) FOX, 'free objects for crystallography': a modular approach to ab initio structure determination from powder diffraction. *J Appl Cryst* 35:734–743
- Favre-Nicolin V, Černý R (2004) A better FOX: using flexible modelling and maximum likelihood to improve direct-space ab initio structure determination from powder diffraction. *Z Krist* 219:847–856
- Fisher RA, Hornung EW (1968) Magnetothermodynamics of $-\text{NiSO}_4 \cdot 6\text{H}_2\text{O}$. III. Derivation of spin-Hamiltonian-molecular-field parameters from experimental data. *J Chem Phys* 48:4284–4291
- Fisher RA, Hornung EW, Brodale GE, Giauque WF (1967) Magnetothermodynamics of $\alpha\text{-NiSO}_4 \cdot 6\text{H}_2\text{O}$. I. Heat Capacity, entropy, magnetic moment, and internal energy, from 0.4° to 4.2°K , with Fields 0–90 kG along the *c* axis. *J Chem Phys* 46: 4945–4958
- Fisher RA, Brodale GE, Hornung EW, Giauque WF (1968a) Magnetothermodynamics of $\alpha\text{-NiSO}_4 \cdot 6\text{H}_2\text{O}$. IV. Heat capacity, entropy, magnetic moment, and internal energy, from 0.4° to 4.2°K , with Fields 0–90 kG along the bisector of the *a,b* axes. *J Chem Phys* 49:4096–4107
- Fisher RA, Brodale GE, Hornung EW, Giauque WF (1968b) Magnetothermodynamics of $\alpha\text{-NiSO}_4 \cdot 6\text{H}_2\text{O}$. II. Heat capacity, entropy, magnetic moment, and internal energy, from 0.4° to 4.2°K , with fields 0–90 kG along the *c* axis. *J Chem Phys* 48:1769–1779
- Fortes AD, Browning F, Wood IG (2012a) Cation substitution in synthetic meridianiite ($\text{MgSO}_4 \cdot 11\text{H}_2\text{O}$) I: X-ray powder diffraction analysis of quenched polycrystalline aggregates. *Phys Chem Mineral* 39: 419–441
- Fortes AD, Browning F, Wood IG (2012b) Cation substitution in synthetic meridianiite ($\text{MgSO}_4 \cdot 11\text{H}_2\text{O}$) II: variation in unit-cell parameters determined from X-ray powder diffraction data. *Phys Chem Mineral* 39: 443–454
- Fortes AD, Fernandez-Alonso F, Tucker MG, Wood IG (2017a) Isothermal equation of state and high-pressure phase transitions of synthetic meridianiite ($\text{MgSO}_4 \cdot 11\text{D}_2\text{O}$) determined by neutron powder diffraction and quasielastic neutron spectroscopy. *Acta Cryst B* 73:33–46
- Fortes AD, Knight KS, Wood IG (2017b) Structure, thermal expansion and incompressibility of $\text{MgSO}_4 \cdot 9\text{H}_2\text{O}$, its relationship to meridianiite ($\text{MgSO}_4 \cdot 11\text{H}_2\text{O}$) and possible natural occurrences. *Acta Cryst B* 73:47–64
- Frazer BC, Brown PJ (1962) Antiferromagnetic structure of CrVO_4 and the anhydrous sulfates of divalent Fe, Ni, and Co. *Phys Rev* 125:1283–1291
- Hashash YMA, Yao JI –C, Wotring DC. (2003) Glyph and hyperstreamline representation of stress and strain tensors and material

- constitutive response. *Int J Numer Anal Method Geomech* 27: 604–626
- Hazen RM, Downs RT, Prewitt CT. (2000) Principles of comparative crystal chemistry. *Rev Min Geochem* 41:1–33
- Henderson CMB, Redfern SAT, Smith RI, Knight KS, Charnock JM (2001) Composition and temperature dependence of cation ordering in Ni–Mg olivine solid solutions: a time-of-flight neutron powder diffraction and EXAFS study. *Am Mineral* 86: 1170–1187
- Hennings E, Zürner P, Schmidt H, Voigt W (2013) Freezing temperatures of aqueous iron(III) sulfate solutions and crystallization of a new acidic water-rich sulfate. *Icarus* 226:268–271
- Hirschmann M (1992) Studies of nickel and minor elements in olivine and in silicate liquids. Ph.D. thesis, University of Washington, Seattle
- Hohenberg P, Kohn W (1964) Inhomogeneous electron gas. *Phys Rev* 136:B864–B871
- Hubbard J (1963) Electron correlations in narrow energy bands. *Proc R Soc Lond Ser A Math Phys Sci* 276:238–257
- Ibberson RM (2009) Design and performance of the new supermirror guide on HRPD at ISIS. *Nucl Instr Methods Phys Res A* 600:47–49
- Ibberson RM, David WIF, Knight KS (1992) The high resolution neutron powder diffractometer (HRPD) at ISIS—a user guide. RAL-92-031. Rutherford Appleton Laboratory, Oxfordshire (<http://www.isis.rl.ac.uk/crystallography/documentation/HRPDguide>)
- Kaminski W (2004) WinTensor 1.1 (<http://cad4.cpac.washington.edu/WinTensorhome/WinTensor.htm>)
- Kohn W, Sham LJ (1965) Self-consistent equations including exchange and correlation effects. *Phys Rev* 140:A1133–A1138
- Larsen AC, Von Dreele RB (2000) General structure analysis system (GSAS). Los Alamos National Laboratory Report LAUR 86-748, Los Alamos, New Mexico <http://www.ncnr.nist.gov/xtal/software/gsas.html>
- Leftwich K, Bish DL, Chen CH (2013) Crystal structure and hydration/dehydration behavior of $\text{Na}_2\text{Mg}(\text{SO}_4)_2 \cdot 16\text{H}_2\text{O}$: a new hydrate phase observed under Mars-relevant conditions. *Am Mineral* 98:1772–1778
- Ma Y, Cheng A-L, Gao E –Q (2010) Ferromagnetic interactions through triple hydrogen bonds in the coordination polymers of α , α' -dihydroxy-bibenzyl-4, 4'-dicarboxylate. *Dalton Trans* 39:3521–3526
- Madsen GK, Novak P (2005) Charge order in magnetite. An LDA + U study. *Europhys Lett* 69:777–783
- Maneva M, Rizova D, Genov L, Liptay G (1990) On the thermal decomposition of $\text{NiSO}_4 \cdot n\text{H}_2\text{O}$ ($n = 7, 6, 4, 1$) and of their deuterated analogs. *J Therm Anal* 36:915–922
- Matsui Y, Syono Y (1968) Unit cell dimensions of some synthetic olivine group solid solutions. *Geochem J* 2:51–59
- McElfresh M (1994) Fundamentals of magnetism and magnetic measurements. Featuring quantum design's magnetic property measurement system. Quantum Design, San Diego
- Momma K, Izumi F (2011) VESTA 3 for three-dimensional visualization of crystal, volumetric and morphology data. *J Appl Crystallogr* 44:1272–1276
- Ottanello G, Della Giusta A, Molin GM (1989) Cation ordering in Ni–Mg olivines. *Am Mineral* 74:411–421
- Payne MC, Teter MP, Allan DC, Arias TA, Joannopoulos JD (1992) Iterative minimization techniques for ab initio total-energy calculations: molecular dynamics and conjugate gradients. *Rev Mod Phys* 64:1045–1097
- Pfrommer BG, Cote M, Louie SG, Cohen ML. (1997) Relaxation of crystals with the quasi-Newton method. *J Comput Phys* 191:233–240
- Ptasiewicz-Bak H, Olovsson I, McIntyre GJ (1997) Charge density in orthorhombic $\text{NiSO}_4 \cdot 7\text{H}_2\text{O}$ at room temperature and 25 K. *Acta Crystallogr B* 53:325–336
- Putz H, Brandenburg K (2006) Diamond—crystal and molecular structure visualization. *Crystal Impact-GbR*, Bonn. (<http://www.crystalimpact.com/diamond>)
- Rajamani V, Brown GE, Prewitt CT. (1975) Cation ordering in Ni–Mg olivine. *Am Mineral* 60: 292–299
- Robinson K, Gibbs GV, Ribbe PH (1971) Quadratic elongation: a quantitative measure of distortion in coordination polyhedra. *Science* 172: 567–570
- Schmidt H, Hennings E, Zürner P, Voigt W (2013) $\text{Fe}_2(\text{SO}_4)_3 \cdot \text{H}_2\text{SO}_4 \cdot 28\text{H}_2\text{O}$, a low-temperature water-rich iron(III) sulfate. *Acta Crystallogr C* 69: 330–333
- Segall MD, Lindan PJD, Probert MJ, Pickard CJ, Hasnip PJ, Clark SJ, Payne MC (2002) First-principles simulation: ideas, illustrations and the CASTEP code. *J Phys Condens Matter* 14:2717–2744
- Senftle A, Thorpe A (1962) Oxygen adsorption and the magnetic susceptibility of ice at low temperatures. *Nature* 194:673–674
- Shannon RD (1976) Revised effective ionic radii and systematic studies of interatomic distances in halides and chalcogenides. *Acta Crystallogr A* 32:751–767
- Stout JW, Hadley WB (1964) Heat capacity of $\alpha\text{-NiSO}_4 \cdot 6\text{H}_2\text{O}$ between 1 and 20°K. Electronic energy levels of the Ni^{++} ion. *J Chem Phys* 40:55–63
- Stout JW, Archibald RC, Brodale GE, Giauque WF (1966) Heat and entropy of hydration of $\alpha\text{-NiSO}_4 \cdot 6\text{H}_2\text{O}$ to $\text{NiSO}_4 \cdot 7\text{H}_2\text{O}$. Their low-temperature heat capacities. *J Chem Phys* 44:405–409
- Takegami S (1922) On the octahydrate of magnesium sulphate. *Mem Coll Sci Kyoto Imperial Univ* 5:191–199
- Thomas EC, Hodyss R, Vu TH, Johnson PV, Choukroun M (2017) Composition and evolution of frozen chloride brines under the surface conditions of Europa. *ACS Earth Space Chem* 1:14–23
- Toby BH (2001) EXPGUI, a graphical user interface for GSAS. *J Appl Crystallogr* 34:210–213
- Toner JD, Catling DC, Light B (2014) The formation of supercooled brines, viscous liquids, and low-temperature perchlorate glasses in aqueous solutions relevant to Mars. *Icarus* 233:36–47
- Tsukimura K, Sasaki S (2000) Determination of cation distribution in $(\text{Co}, \text{Ni}, \text{Zn})_2\text{SiO}_4$ olivine by synchrotron X-ray diffraction. *Phys Chem Minerals* 27:234–241
- Viola C (1923) Über bestimmte Mischkristalle. *Z Kristallogr* 58:583–595
- Vokurka K, Rieder M (1987) Thermal-expansion and excess volumes of synthetic olivines on the $\text{Mg}_2\text{SiO}_4\text{-Ni}_2\text{SiO}_4$ join. *Neues Jahrb Min Monatsh H3*: 97–106
- Vu TH, Hodyss R, Choukroun M, Johnson PV (2016) Chemistry of frozen sodium–magnesium–sulfate–chloride brines: implications for surface expression of Europa’s ocean composition. *Astrophys J Lett* 816:L26
- Vu TH, Hodyss R, Johnson PV, Choukroun M (2017) Preferential formation of sodium salts from frozen sodium-ammonium-chloride-carbonate brines—Implications for Ceres’ bright spots. *Planet Space Sci* 141: 73–77
- Watanabe T (1962) Magnetic properties of $\text{NiSO}_4 \cdot 7\text{H}_2\text{O}$ and $\alpha\text{-NiSO}_4 \cdot 6\text{H}_2\text{O}$ at low temperatures. *J Phys Soc Jpn* 17: 1856–1864
- Wood IG, Hughes N, Browning F, Fortes AD (2012) A compact, transportable, thermoelectrically cooled cold stage for reflection geometry X-ray powder diffraction. *J Appl Crystallogr* 45:608–610
- Wu Z, Cohen RE (2006) More accurate generalized gradient approximation for solids. *Phys Rev B* 73:article 235116

Affiliations

A. D. Fortes^{1,2}  · K. S. Knight^{1,2,3} · A. S. Gibbs¹ · I. G. Wood²

¹ ISIS Facility, STFC Rutherford Appleton Laboratory, Harwell Science and Innovation, Campus, Chilton, Didcot, Oxfordshire OX11 0QX, UK

² Department of Earth Sciences, University College London, Gower Street, London WC1E 6BT, UK

³ The Natural History Museum, Cromwell Road, London SW7 5BD, UK